Superconductivity in carbon nanotubes

Junji Haruyama[1-3]
[1]*Aoyama Gakuin University, 5-10-1 Fuchinobe, Sagamihara, Kanagawa 229-8558, Japan*
[2]*Institute for Solid State Physics, University of Tokyo, Kashiwanoha 5-1-5, Kashiwa, Chiba 277-8581, Japan*
[3]*Japan Science and Technology Agency-CREST, 4-1-8 Hon-machi, Kawaguchi, Saitama 332-0012, Japan*

Abstract

Carbon nanotubes (CNTs), which are one-dimensional (1D) molecular conductors, have attracted considerable attention from viewpoints of the novel structures, electronic states, quantum phenomena, and also applications to new opt and electronic devices. However, mostly none reported on superconductivity (SC) and its correlation with 1D electron phenomena. In the present study, I report on SC with the world-highest transition temperature (T_c) of 12K (1) in arrays of multi-walled CNTs (MWNTs) with entirely end-bonded electrode junction and (2) in highly uniform thin films of boron-doped single-walled CNTs (*B*-SWNTs). In the former one, I reveal correlation of SC with Tomonaga-Luttinger liquid (TLL) state, which is a collective phenomenon arising from repulsive Coulomb interaction between electrons confined in 1D ballistic charge transport regimes. In the latter one, I clarify correlation of SC with van Hove singularities (VHS) in electronic density of states (DOS) in the SWNT. Based on this thin film, I show fabrication of paper-like thin films consisting of pseudo two-dimensional network of weakly coupled *B*-SWNTs (the so-called Buckypaper) and show an enhancement of the onset T_c up to 19 K by applying only a small pressure. In section 4, I discuss about possibility for realization of quantum spin entangler and quantum bit utilizing a hybrid system of CNTs/superconductor, which is associated with the section 1. Because CNTs have strong spin coherence and possibly strong spin entanglement in spin singlet (Cooper pair), it must allow realization of quantum spin entangler and bit without decoherence problem in near future. The present observations will shed light to feasibility of CNTs as a 1D superconductor and also research of 1D electron correlation. They promise application to novel quantum devices.

1. Superconductivity in multi-walled carbon nanotubes: Interplay of Tomonaga -Luttinger liquid and superconductive phase

It is well known that the phonon- mediated attractive electron-electron interaction leads to a superconductive instability in 2D and 3D conductors. In particular, high-Tc SC favors 2D space such as cupper-oxide high-T_c superconductors. Here, how does SC like 1D space? In CNTs, which is one of typical 1D conductors, a variety of 1D quantum phenomena have been reported. However, intrinsic SC has been reported in the CNTs only by a few groups [1-3]. Nevertheless, the SC in a CNT is attracting considerable attention for the following reasons: (1) The curvature resulting from a small diameter (<< ~1 nm) can bring high a T_c due to a strong coupling of σ-π band electrons, which arises from formation of sp^3 hybrid orbitals and σ-π mix band, with radial breathing phonon mode. (2) The perfect alignment of the Fermi level (E_F) to a van Hove singularity (VHS) can also lead to high T_c due to the appearance of an extremely large electronic density of states (DOS). (3) It can provide an insight into the 1D electron correlation. Thus, study of SC in CNTs can shed lights to feasibility of 1D conductors as superconductors.

In contrast, many quantum phenomena and electronic states tend to obstruct appearance of SC in 1D space. For instance, Coulomb repulsion in TLLs, energy gaps arising from Pierls transition, very small electronic DOS in energy regimes out of VHSs, and phase fluctuation can such obstructions. In particularly, TLL is one of typical 1D quantum phenomena. The TLL provides the relevant theoretical description [4–6], representing a collective electronic state (e.g., showing spin-charge separation) that arises from the repulsive Coulomb interaction between electrons confined in a 1D ballistic conductance regime. Many previous works have reported TLL features in CNT systems. It is known that the tunneling density of states ν(E) for the TLLs decreases following a power-law dependence on energy, $\nu(E) \propto E^{\alpha}$, where the power α is given by different expressions according to the different tunneling regimes [4, 5, 12]. Most previous works on CNTs have been dealing with the regime of strong Coulomb interaction.

Here, SC is a phenomenon arising from attractive Coulomb interaction via phonon, which is in contradiction to the Coulomb repulsion leading to the TLL state. This leads naturally to the question of how the SC can develop in the CNTs, with the consequent transition from the TLL [7–11, 14]. The interplay between the TLL state and intrinsic SC has been only reported in our MWNTs with a significant number *N* of shells participating in the conduction [2]. The results were qualitatively consistent with low-energy theories of CNTs [8], which had already predicted the breakdown of the TLL at low temperatures in nanotube bundles with a strong intertube electrostatic coupling between the different 1D conduction channels.

In the MWNTs, however, the interplay of the SC with the TLL and the value of T_c as high as 12 K still had to be quantitatively understood, as the samples were not intentionally doped and the number of 1D conduction channels was unknown. On the other hand, the high T_c value was in approximate agreement with T_c's = ~10K of CaC_6 and boron(*B*)-doped diamond. Indeed, low-energy theories of MWNTs have suggested the importance of having a large number of 1D conduction channels for the development of a SC instability [10]. Therefore, it is crucial to clarify the correlation between the appearance of the SC phase and carrier doping in MWNTs. *B*-doping has been actually successfully achieved following known methods [15, 16].

In this section, I report on SC in array of the MWNTs and reveals correlation with TLL state. I find an abrupt resistance drop due to SC at a T_c as high as 12K in the entirely end-bonded MWNTs. In contrast, the partially end-bonded MWNTs show very small resistance drop at low temperatures. It reveals that a gradual transition from TLL behavior to a SC regime can start only from low *eV/kT* values at low temperatures, but the development of the SC enhances the regime to high *eV/kT* region. Phase diagram obtained from low-energy theory reveals that such a transition is actually possible. Nuclear Magnetic Resonance (NMR) measurements ascertain the presence of substitutional boron doping for SC in the MWNTs.

At first, I report on the possibility of unintentional *B*-doping in our MWNTs, which were synthesized by chemical vapor deposition using Fe/Co catalyst and methanol gas in the nanopores of the alumina template [2, 19]. Boron has been intentionally used only for the enhancement of the chemical reaction of the Fe/Co catalyst [2, 19]. Figure 1 shows results of nuclear magnetic resonance (NMR) measurements of our MWNTs with three different boron concentrations (N_B) in the catalyst. Evident peaks can be observed at 0 ~ 5 ppm in individual samples. The peak position implies the presence of chemical bonds of *B-C* and, hence, substitutional *B* doping in the carbon network of the MWNTs. Moreover, at least five-times higher intensity of NMR signal peak for the *B-C* was detected in the *B*-MWNTs with N_B = ~2 at.%, compared with other *B*-MWNTs with different N_B values. Very importantly, we find that only the *B*-MWNTs with N_B = ~2 at.% showed SC with high T_c (Fig. 3(a)) and also present signature of SC (Fig. 3(b)) with the highest reproducibility. This result implies that the most suitable condition for substitutional *B* doping into the MWNTs, which leads to appearance of the SC, is ~2 at.%. This is consistent with our recent discovery [20] and a theory [21]. The small *B* concentration allows the CNTs remaining a 1D ballistic charge transport regime.

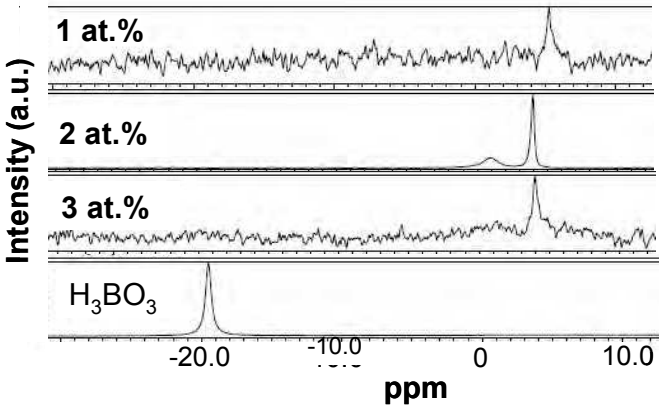

Fig. 1. NMR measurement results of the MWNTs that were synthesized from Fe/Co with different *B* concentration noted by atomic %, using ^{11}C. Result of H_3BO_3 is a reference. H_3BO_3 was mixed in $FeSO_4$ and $CoSO_4$, and then Fe/Co catalyst including *B* was electrochemically deposited into the bottom ends of nanopores of alumina template [5, 19].

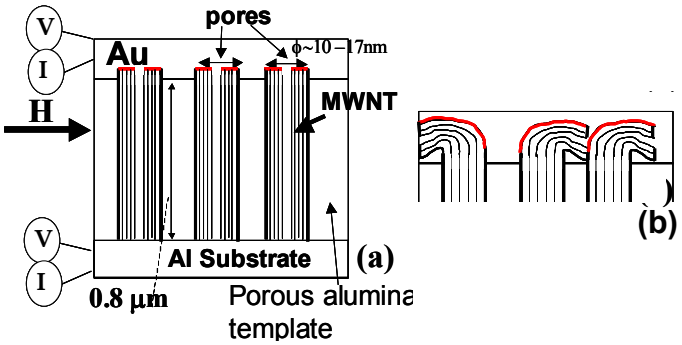

Fig. 2. Schematic cross sections of array of MWNTs with (a) entirely end-bonded and (b) partially end-bonded junctions between Au electrode and top ends of MWNTs. The red lines indicate the interfaces between the MWNTs and the electrodes.

Figure 2 shows the schematic cross sections of our samples, which include arrays of *B*-MWNTs with (a) entirely end-bonded (N = 9) and (b) partially end-bonded ($1 < N < 9$) junctions to Au electrodes [2]. They were fabricated by entirely and partially cutting the excess top portions of MWNTs, which were grown up from the nanopores and accumulated on alumina membrane, respectively. No cutting resulted in bulk junction, which has electrical contact to only the outermost shell (i.e., N = 1).

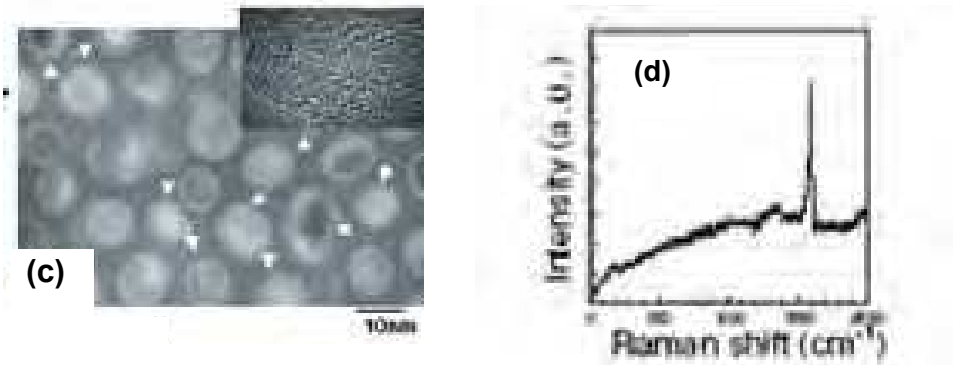

Fig. 2. (c) Plane TEM image of an array of MWNTs. Inset: High resolution TEM image of one MWNT. (d) Resonant Raman spectrum of the MWNT. The significantly sharp peak indicates G band.

Figure 2(c) shows a planer TEM image of the sample [2]. One can confirm presence of MWNTs in most pores. Figure 2(d) shows measurement result of resonant Raman spectrum. Peak height of G band is significantly greater than that of D band. This strongly indicates high quality of the MWNTs.

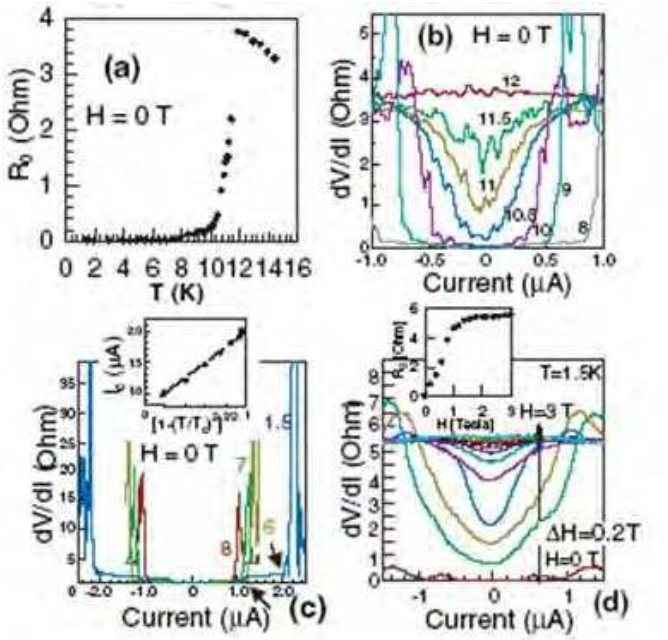

Fig. 3. (a) Superconductivity with T_c=12K in the sample with junction type (a) (b) Differential resistance vs. Temperature (Kelvin) for (a) (T>8K). (c) that for T<8K Inset : Critical current vs. Normalized temperature for GL theory (d) Differential resistance vs. magnetic fields applied perpendicular to tube axis

Figure 3 shows superconducting behaviors of the entirely end-bonded MWNTs as shown in Fig. 2(a). In Fig. 3(a), zero-bias resistance (R_0) abruptly starts to drop from T_c = 12K and attains to zero-ohm at T = 7.8K, when residual resistance, which arises from contact resistance, was subtracted. Figure 3(b) shows the differential resistance dips for various temperatures > 8K. As temperature decreases, the dip monotonically deepens and mostly attains to zero-ohm at the center point at T = 8K. This is consistent with Fig. 3(a). Figure 3(c) shows differential resistance at T < 8K. When current increases at each temperature, zero differential resistance dip suddenly disappears at critical current (I_c). The inset shows relationship of I_c vs. temperature normalized for GL equation. It exhibits a linear relationship and turns out that Figs.3(a) – (c) are attributed to SC. Figure 3(d) shows differential resistance dips as a function of magnetic field. The dip rapidly disappears as the field increases.

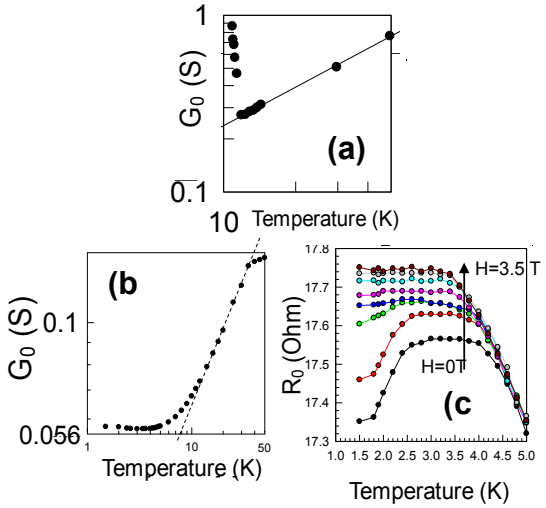

Fig. 4. Doubly logarithmic scales of zero-bias conductance G_0 and temperature for (a) entire and (b) partial end junctions. (c) Magnetic field dependence of zero-bias resistance R_0 as a function of the temperature, corresponding to (b).

Figure 4 shows the doubly logarithmic scales of zero-bias conductance G_0 and temperature for the two different junctions shown in Fig. 2. The observed power law behaviors in the different types of junctions ($G_0 \propto T^{\alpha}$; α = 0.7 and 0.8 in (a) and (b) respectively) are in excellent agreement with the previous reports of TLL behavior in CNTs [2, 5]. As shown in Fig. 4(a), the abrupt G_0 increase (i.e., SC regime) appears overcoming the TLL behavior (i.e., the power law at T > 12K) at T_c = 12 K in the entirely end-bonded *B*-MWNTs. The origin of this effect was in the large screening of the Coulomb interaction, arising from the electrostatic coupling between a large number of 1D conduction channels due to boron doping and also the large *N* value originating from entire end-bonding of the *B*-MWNTs [2, 8].

In contrast, in the partially end-bonded *B*-MWNTs, only a slight and gradual G_0 increase at T < 2.5K (i.e., a signature of SC correlations) can be observed as shown in Fig. 4 (b). As we implied in ref. [5], the appearance of SC and the correlations of power laws with G_0 increase were strongly correlated with the values of *N* as shown in Fig. 3. Because we could confirm that the abrupt G_0 increase in Fig. 4(a) was attributed to SC as mentioned above [2], it can be concluded that the small G_0 increase observed in Fig. 4(b) is also attributed to SC. The gradual G_0 increase corresponds to the slight and gradual resistance drop shown in Fig. 4(c). With an increase in the magnetic field, the drop in R_0 disappears rapidly. This behavior actually agrees with that of conventional superconductors.

In Fig. 4(b), the power law is observable up to T = ~40 K for α = ~0.7, while it gradually starts to deviate below T = ~12 K. At T < ~6 K, it saturates completely. Subsequently, a small increase in G_0 due to the SC correlations appears at T < ~2.5 K. However, the trend towards the SC transition is not completed above T = 1.5 K in this case. This is consistent with the fact that the SC phase requires the coherent transport of Cooper pairs along the directions transverse to the CNTs, which cannot be established when only part of the shells are

electrically active and the number of conductance channels is smaller as in the partially end-bonded *B*-MWNTs with the small *N* values [2, 8]. This also implies that the Coulomb interaction cannot be sufficiently screened to allow for the development of SC correlations. In fact, *B*-MWNTs with $N = 1$ exhibited no G_0 increase, consequent with the absence of screening of the Coulomb interaction.

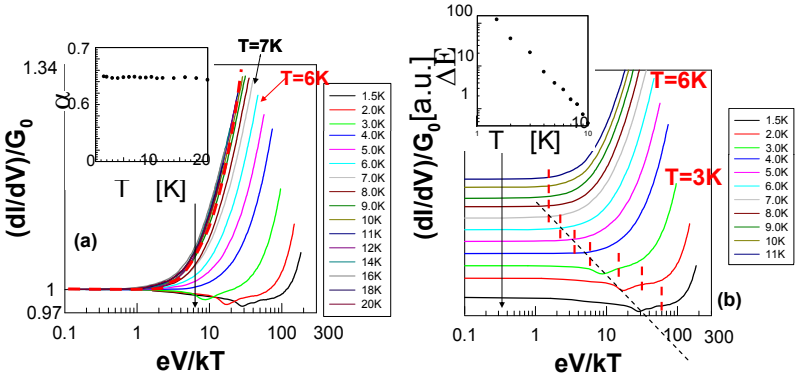

Fig. 5. **(a)** Doubly logarithmic scales on normalized differential conductance vs. *eV/kT*, corresponding to TLL formula in $eV >> kT$ regime [13]. The red dotted line gives the best fitting result by eq.(1). **Inset**: power value α vs. temperature estimated from main panel. **(b)** Transform of $(dI/dV)/G_0$ in Fig. 5(a) to arbitrary units. The long black-dotted line connects the right edges of the conductance peaks. **Inset**: ΔE_c vs. temperature on doubly logarithmic scales. $\Delta E_c = E_c(T) - E_c(T = 7\ K)$, where $E_c(T)$ is the boundary point between the saturation and power law regions at each temperature, as shown by the short red-dotted lines in the main panel.

On the other hand, besides the dependence on temperature, the power law behavior of the observables as a function of the bias voltage *V* provides absolute evidence of the TLL behavior [4, 5, 13]. Thus, it is crucial to investigate the regime $eV >> kT$ to discuss in depth the transition from TLL behavior to the SC phase. In this sense, Fig. 5(a) exhibits doubly logarithmic plots of the normalized differential conductance vs. *eV/kT*, which is one of the typical dependences to check the TLL behavior for $eV >> kT$ [13]. It shows that the entire data collapse suitably onto a single universal curve at $T \geq \sim 7$ K. This agrees with the results reported in previous investigations of TLL behavior [4, 5, 13]. As shown by the red dotted line, this universal curve can be fitted by the following result for a TLL [13]

$$\frac{G(V,T)}{G(V=0,T)} = \cosh(\gamma\frac{eV}{2kT})\frac{1}{\left|\Gamma(\frac{1+\alpha}{2})\right|^2}\times\left|\Gamma(\frac{1+\alpha}{2}+\gamma\frac{ieV}{2\pi kT})\right|^2 \quad (1)$$

where V is the applied voltage; $\Gamma(x)$, the Gamma function; k, the Boltzmann constant; and γ, the inverse number of the measured junctions M weighted by their resistance [13]. For M junctions in series, the value of γ should be within $\gamma = 1/M$. The best fit gives the parameter γ = ~0.7, which is mostly in good agreement with $\gamma = 1/M = 0.5$ for $M = 2$ of our individual MWNTs with two end junctions. Therefore, we conclude that the universal curve can be actually attributed to TLL behavior at $T \geq$ ~7 K [2].

However, we importantly find appearance of a deviation from the universal curve in the low temperature regime (e.g., at $T \leq 6$ K) in Fig. 5. As shown by red lines in Fig. 5(b), this deviation originates from a monotonic increase in the width of the low-eV/kT saturation region (i.e., $eV/kT <$ ~2 at T = 6 K) in the universal curve at $T \leq$ ~6 K. The inset of Fig. 5(b) shows ΔE_c (width of the saturation region) as a function of temperature in a doubly logarithmic scale. Indeed, we can confirm that ΔE_c actually increases with a decrease in temperature, following power law dependence.

Quite remarkably, it should be noted that the value of the critical temperature of 6 K for the deviation of the universal curve is in excellent agreement with that of the saturation region in Fig. 4(b). This agreement strongly suggests that the deviation at $T \leq$ ~6 K in Fig. 4 for $eV >> kT$ is associated with the appearance of the SC regime. Figure 5(b) supports this argument, because it suggests that the increase in the width of the saturation region is caused by the appearance (insertion) of the conductance peak due to emergence of the SC regime. In particular, this is evident at $T \leq 3$ K, where G_0 is seen to increase in Fig. 4(b) [22]. This implies that the emergence of the SC regime at low eV/kT leads to the deviation from the TLL states [17].

In the conventional theory of a TLL, the width of the low-eV/kT saturation region (< ~1) reflects the regime of $eV/kT < \Delta E = h\nu_F/L$, where ΔE is the energy spacing of the quantized electronic orbital formed in the CNTs in the ballistic charge transport regime [18]. This means that the noise from thermal fluctuations smears the effects of the bias voltage (i.e., power laws) out in the low-eV/kT regime (< ~1). In contrast, one should notice that insertion of the conductance peak in Fig. 5(b) enhances this thermal smearing region to high-eV/kT regime (~100) at T = 1.5 K. This is very anomalous and, hence, strongly implies a possibility that appearance of the SC regime introduces superconducting gap Δ_{SC} in the system, resulting in $\Delta E + \Delta_{SC}$.

Moreover, the inset of Fig. 5(a) shows the values ofα, which were estimated from the main panel of Fig. 5(a), as a function of temperature. It is very important to note that the α value is constant (~0.67) in all the temperature range, despite the emergence of conductance peak due to the SC regime at low eV/kT regime below T = 6K. This implies that the transition from the TLL behavior to the SC regime starts to occur only in the low eV regime, when the values of eV are drastically lowered under constant low kT values.

Here, in Fig. 6, we show that such a transition is actually possible on the light of the low-energy theories of doped MWNTs [10]. The two regimes are represented in the phase diagram of Fig. 6, which has been obtained following the approach of Ref. [10]. We observe that a minimum N value per shell (10) in a MWNT is needed for the onset of the SC regime, and that subsequent peaks arise in the critical temperature as the Fermi level(ε_F) crosses the top of a new subband (i.e., a Van Hove singularity). This result is in good agreement with the present experimental results, in which the N_B value is below 2 at.% with the small N values leading to shift of ε_F in ~0.3 eV [20, 21] and corresponding T_c of 3 ~ 12K.

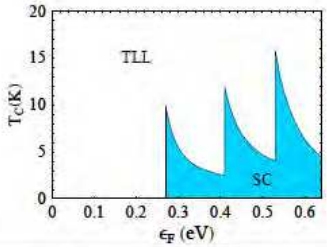

Fig. 6. Phase diagram of doped MWNTs (incorporating the average over different geometries of the shells) in terms of the doping level, represented by the shift in the Fermi energy ε_F with respect to the charge neutrality point, and the temperature].

The characterization of doping in the MWNTs provides actually the clue to account for the SC regime. This appears as a consequence of the large screening of the Coulomb interaction, which arises in doped MWNTs, as in the case of CNT ropes [8], from the electrostatic coupling of a large number of 1D conduction channels. The effect is such that the long-range part of the Coulomb potential is largely suppressed, placing the system on the verge of a pairing instability. This takes place as the intertube Cooper-pair tunneling is progressively enhanced at low energies [10]. In this respect, the Cooper pairs do not find the obstruction that single electrons have to tunnel between the incommensurate CNT lattices of a MWNT. When intertube coherence can be established at some low temperature T_c under a low eV value, the system undergoes the transition from the TLL to the SC regime as shown in Fig. 6. Although further quantitative investigation is expected, the present phenomena must shed light on understanding of interplay of SC with 1D electron correlations in *B*-CNTs.

2. Superconductivity in thin films of boron-doped carbon nanotubes

New carbon-based superconductors - calcium- intercalated graphite (C_6Ca) and highly boron *(B)*- doped diamond [23-*25*] - have been discovered recently and have attracted attention. It is well known that the small mass of carbon can promote high T_c in Bardeen-Cooper-Schrieffer (BCS)-type SC and novel behaviors of SC can also be expected. As mentioned in section 1, the SC in a CNT is attracting significant attention [26-*30*] for the following reasons: (1) The curvature resulting from a small diameter can bring high T_c due to a strong electron-phonon coupling [31]. (2) The alignment of the E_F to a VHS can also lead to high T_c due to the presence of an extremely large DOS [31]. (3) It can provide an insight into the 1D electron correlation [29, 32-*36*].

Here, it is also a well-known fact that effective carrier doping is crucial for realizing high-T_c SC in any material. In fact, SCs in C_6Ca and *B*-diamond have been associated with it. Carrier doping into CNTs has also been studied in many previous works [37-*39*]. Ref.[37] have reported a systematic study of SWNT bundles using the pulsed laser vaporization technique, in which the *B* doping concentration (N_B) is controlled by the amount of elemental *B* mixed into a Co/Ni catalyst impregnated targets. Evidence for substitutional *B* doping and enhanced electronic DOS at the E_F has been reported previously [37-*39*].

Nevertheless, experimental studies on the SC in carrier-doped CNTs are lacking. Although only I reported on SC in the *B*-MWNTs as explained in section 1, the boron doping was accidental and could not be in a controlled manner. This could be due to (1) difficulties

associated with substitutional doping in CNTs (with diameter as small as ~1 nm) without compromising structural integrity of the hexagonal carbon network, (2) since the conventional size of Cooper pairs and the path of the Meissner shielding current cannot be smaller than 1 nm, SC cannot be realized in an isolated single CNT [30], (3) in individual CNTs, strong 1D electron correlation phenomena tend to destroy Cooper pairs and the alignment of the E_F to a VHS requires highly optimized doping rate. From these viewpoints, the assembled *B*-doped SWNTs with low *B* concentration reported in this section are crucial for the observation of Meissner effcet [30, *33, 46*]. Theoretical studies also suggests that SC can be realized in *B*-SWNTs due to small-dopant-induced (≤ 0.4 at. %) tuning of the E_F with the VHS present in individual (10, 0) SWNTs [40] and also in carrier-doped MWNTs [36].
In this section, I report on SC in the thin films of *B*-SWNTs and clarify correlation with VHS in electronic DOS in 1D conductor. I report on the Meissner effect and show that only SWNT films consisting of low boron concentration leads to evident Meissner effect with T_c = 12 K. I also show that a highly homogeneous ensemble of the SWNTs is crucial for realizing the Meissner effect. The first-principles electronic-structure study of the *B*-SWNT reveals strongly correlation of the boron concentration for Meissner effect with VHSs.

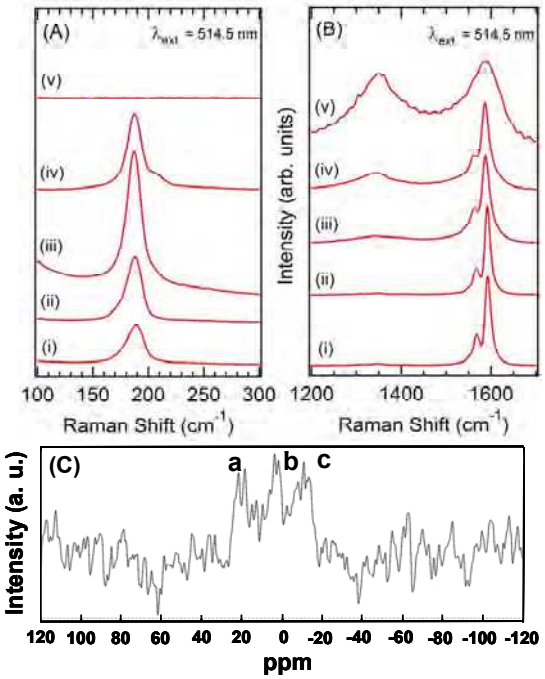

Fig. 7. (a)(b) Room temperature Raman spectra of semiconducting *B*-SWNT bundles synthesized from targets containing boron concentrations (N_B) of ~ (i) 0 (ii) 1.5 (iii)2.0 (iv) 3.0 (v) 4.5 atomic %. An excitation wavelength λ_{ex} = 514.5 nm is used to probe the *B*-induced changes in the Raman spectra. The *B*-induced changes in (a) the *RBM* (present around 200 cm^{-1}) and (b) the *D* band (present around 1300–1350 cm^{-1}) are shown. (c) Result of NMR measurement of *B*-SWNTs synthesized with N_B = ~1.5 at. % target. Three peaks noted as a, b, and c are evidently observed.

Figure 7 (a) and (b) show the room-temperature Raman spectra of semiconducting SWNT bundles prepared from targets containing *B* in the range $0 < N_B < 4.5$ at. % (described above and in Ref. [37, *46*]). The present catalytically *B*-doping method allows *B* doping in low concentration in the SWNTs, avoiding destruction of carbon networks. The data set shown in Fig. 7 clearly reveals the following: (1) In Fig. 7(a), the intensity of the radial breathing mode (*RBM*) varies nonlinearly with the N_B and exhibits the highest values around $N_B = 1.5$ and 2 at. %. These intensity changes result from a change in the resonance conditions induced by the presence of *B* in the SWNT lattice, which shifts the transition energies between the VHSs in the electronic DOS. (2) No SWNTs are present in the products prepared from targets with N_B in excess of 4 at. %, since the *RBM* is absent in their spectra in Fig. 7(a). This decline is strongly correlated with the well-known saturation limit of ~4 at. % for N_B in graphite at 1200 K. (3) In Fig. 7(b), a systematic increase in the intensity of the disorder-induced band (*D* band) with increasing N_B is evident implying that a change in the degree of ordering in the hexagonal lattice of the SWNTs results due to the incorporation of *B* in the lattice. Similar results are observed in the bundles of metallic SWNTs.

Figure 7(c) shows the result of nuclear magnetic resonance measurement (JNM-ECX400) of *B*-SWNTs synthesized target with $N_B = 1.5$ at. %. It evidently exhibits presence of three peaks (a, b, and c). The peaks noted as *b* and *c* originate from chemical bonds between *B* and carbon, in which the peak heights are highly sensitive to *B* concentration in the target. In contrast, peak *a* originates from *B*-oxide bond. The thermoelectric power (TEP) measurements also provide complementary evidence for the *B*-induced changes in the electronic properties since temperature dependent TEP studies revealed *p*-type characteristics [37]. These results collectively provide strong evidence for substitutional doping of *B* in the SWNTs.

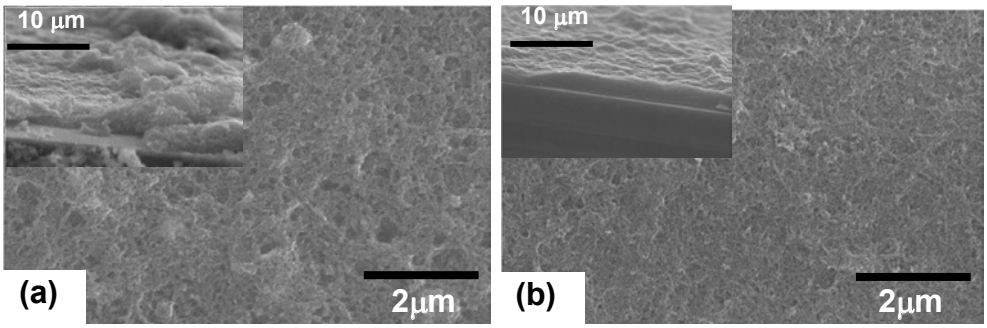

Fig. 8. Scanning electron microscope (SEM) images of thin films consisting of assembled *B*-SWNTs prepared on Si substrates. (a) Film fabricated without spin coating and (b) film fabricated by spin coating (500 rpm). Insets: Cross-sectional SEM images of individual samples observed at a 30° tilt.

The magnetization measurements of the thin films consisting of *B*-SWNTs [40] were performed using a superconducting quantum interference device (Quantum Design, MPMS) [24]. Figure 9 shows normalized magnetization ($M_N = M(T) - M(T=40K)$) as a function of the temperature (*T*) (M_N–*T* relationship) in field-cooled (FC) and zero-field -cooled (ZFC) regimes in the highly uniform film with $N_B \sim 1.5$ at. % as shown in Fig. 8(b) . Evident drop in

M_N is observed below T_c = 12 K in the ZFC regime, and below T = ~8 K in the FC regime. Interestingly, this value of T_c = 12 K exactly agrees with the T_c value for an abrupt resistance drop observed in the array of entirely end-bonded MWNTs [29]. The small M_N drop observable at T_c > 12 K in the ZFC regime is due to diamagnetism of graphite structure of bundle of SWNTs and not associate with Meissner effect [41]. It is found that the magnitude of the drops observed in the M_N–T relationship becomes considerable at magnetic field (H) < ~1400 Oe as H values increase. In contrast, it decreases for H > ~1400 Oe, and at H = ~3500 Oe, the magnitude becomes almost zero.

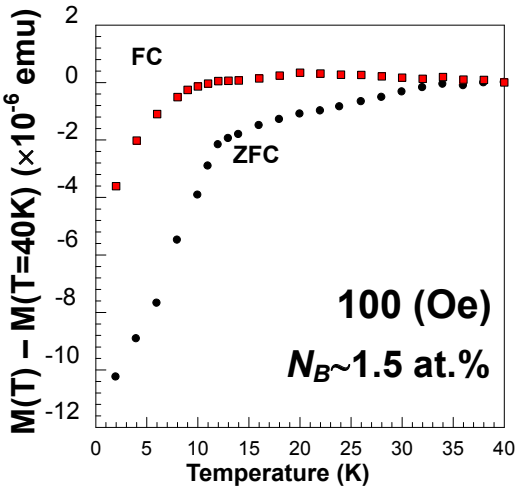

Fig. 9. Normalized magnetization as a function of temperature at magnetic fields (H) of 100 Oe in FC and ZFC regimes in thin films of assembled B-SWNTs, which are synthesized from a target with N_B = ~1.5 at. %. The films are prepared on a Si substrate by spin coating at 500 rpm.

Figure 10 shows the values of M_N as a function of H (M_N–H relationship) for various T in the ZFC regime in the sample shown in Fig. 9. At each temperature, M_N values decrease at H < ~1400 Oe, while they increase at H > ~1400 Oe. The magnitude of the drops decreases monotonically as T increases. These behaviors observed in the shown M_N–T and M_N–H relationships are qualitatively in good agreement with the Meissner effect in type-II superconductors.

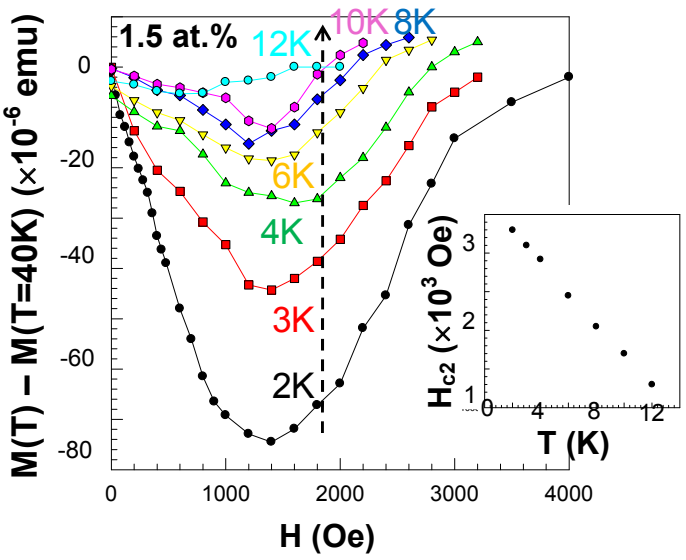

Fig. 10. Normalized magnetization vs. magnetic field for various temperatures in the sample shown in Fig. 9. **Inset:** Upper critical field (H_{c2}) vs. temperature relationship estimated from main panel. We determine H_{c2} at the H value for which M_N = 0 at each temperature by extrapolating the linear slope of the M_N–H relationship for H > ~1500 Oe in main panel.

In order to confirm the Meissnser effect, we focus on the temperature dependence of the upper critical magnetic fields (H_{C2}) in the M_N–H relationships shown in Fig. 10. The inset of Fig. 10 shows the result of the relationship between the estimated H_{c2} and T. The values of H_{c2} decrease linearly as the temperature increases. This result is also qualitatively in good agreement with the results for type-II superconductors. Residual H_{c2} around T_c = 12K is attributed to diamagnetism of graphite as mentioned above.
From a quantitative viewpoint, the values of H_{c2} (T = 0) = ~1700 Oe can be estimated from the inset of Fig. 10 and the relationship

$$H_{c2}(T = 0) = -0.69(dH_{c2}/dT\,|_{Tc})\,T_c \quad (2)$$

$$dH_{c2}/dT\,|_{Tc} = -200 \text{ and } T_c = 12 \text{ K} \quad (3).$$

The Ginzburg-Landau (G-L) superconductive coherence length

$$\xi = [\Phi_0/2\pi H_{c2}(T = 0)]^{1/2} \quad (4)$$

where $\Phi_0 = h/2e$ is the quantum magnetic flux, can be estimated as ξ = ~ 17 nm from the H_{c2} (T = 0) = ~1700 Oe. Further, the penetration length of the magnetic field

$$\lambda = (m^*/\mu n_s e^2)^{1/2} \quad (5)$$

is estimated to be of the order of ~100 nm. This λ value is significantly larger than ξ = ~ 17 nm. This result apparently supports the fact that the present films of *B*-SWNTs are type-II superconductors. Moreover, the value of ξ = ~ 17 nm is in good agreement with ξ = ~11 nm in the arrays of MWNTs [*8*], ξ_{ab} = 13 nm in C_6Ca [23, 24], and ξ = 10 nm in *B*-doped diamond [25]. Therefore, we conclude that the M_N–*T* drops shown in Fig. 3 and the corresponding M_N–*H* relationship shown in Fig. 10 are attributed to the Meissner effect observed in type-II superconductors. The gradual and unsaturated M_N drops in the Meissner effect imply inhomogeneous *B* doping similar to the cases of C_6Ca and *B*-diamond at early stage.

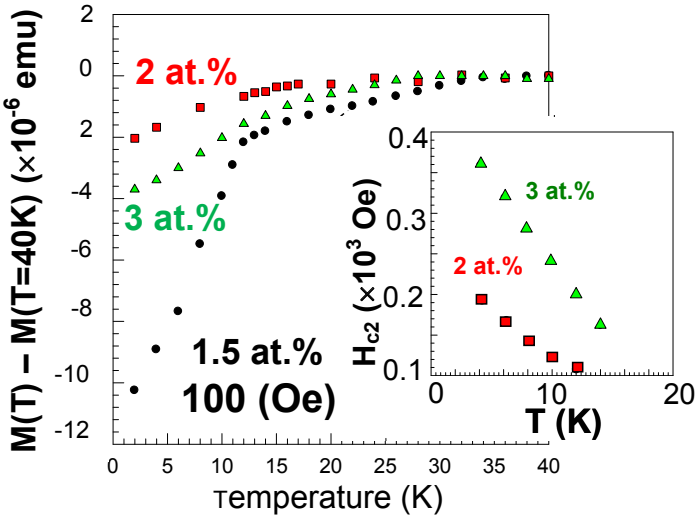

Fig. 11. Correlation of normalized magnetization drops with N_B in targets. Contribution of graphite structure on magnetization is not subtracted.
Inset: H_{c2} vs. temperature relationships estimated from M_N–*H* relationship in the thin films consisting of high N_B –value SWNTs (2 and 3 at. %).

Here, we find that appearance of the Meissner effect is extremely sensitive to degree of uniformity of the thin *B*-SWNT films, which can be controlled by the conditions used in the spin coating process [40]. Figure 8 shows the SEM top view and cross-sectional images (observed at a tilt of 30 degree) of the thin films consisting of assembled *B*-SWNTs fabricated without spin coating (a) and by spin coating at 500 rpm (b). The difference in the uniformities of the thin films shown in Figs. 8(a) and (b) is very evident. Further, in the case of spin coating at 1000 rpm, the extremely large number of rotations results in poor uniformity, similar to Fig 8(a). All 10 samples fabricated by the spin coating at 500 rpm exhibit the evident Meissner effect, as shown in Figs. 9 and 10. In contrast, in the samples fabricated without spin coating and by spin coating at 1000 rpm, only one sample out of 20 exhibits the Meissner effect. This result suggests that the Meissner shielding current or a superconducting vortex is not confined to individual SWNTs but exists across assembled

B-SWNTs in the thin films. Indeed, ref.[42] has predicted that Cooper pairs have a conducting probability across assembled SWNTs (with different chilarity) higher than that in individual electrons This suggestion is also consistent with ξ = ~17 nm mentioned above, because ξ corresponds to the diameter of Cooper pair and the diameter of individual SWNT is ~1 nm at most.

Figure 11 shows the correlation of the M_N–T and M_N–H behaviors with the N_B values in the catalyst in the ZFC regime. It clearly indicates strong sensitivity to N_B; i.e., (1) the M_N drops become considerably smaller and ambiguous [41] in the samples with N_B values of 2 at.% and 3 at.% as compared to those with N_B = 1.5 at.% and (2) the M_N drop in the sample with N_B = 2 at.% is slightly more than that with N_B = 3 at.%. The M_N–H relationships similar to that shown in Fig. 10 were found in the samples with N_B = 2 and 3 at.%. However, the H_{c2} values of the order of 100 Oe as shown in the inset of Fig. 11 are considerably smaller than those of the order of 1000 Oe shown in Fig. 10. The estimated values of H_{c2} (T = 0) = ~280 Oe and ξ = ~7 nm for the N_B = 3 at.% sample are also considerably smaller than the corresponding values in the N_B = 1.5 at.% sample (H_{c2} (T = 0) = ~1700 Oe and ξ = ~17 nm). These results imply that low *B* concentration yields stronger SC behavior. This is mostly consistent with the intensity change in the *RBM* as shown in Fig. 7, which exhibited the highest intensity around 1.5 and 2 at. %.

This result is also qualitatively in good agreement with the first-principles electronic-structure study of the *B*-SWNT [43]. From the electronic band structure and DOS of (10,0) SWNT with N_B values of 0.83 at.% to 2.50 at.%, it can be predicted that the occurrence of SC should be sensitive to the correlation of the position of the Fermi level with that of the VHS, and that even lower N_B value should be preferable for realizing SC as shown in inset of Fig. 12. Main panel of Fig. 12 shows the electronic structure of BC_{159} which corresponds to the N_B value as low as 0.625 at.% using the local-density approximation in the framework of the density functional theory [44]. It clarifies that the Fermi-level DOS of this system is considerably larger than those of higher N_B -value systems [45].

A resistance drop has not yet been detected owing to very high resistance (>> ~MΩ), because of (1) difficulty in establishment of good ohmic-contact between individual SWNTs and metal electrodes, (2) impossibility in having just a single *B*-SWNT aligned within the 1 μm electrode spacing since the maximum length of most SWNTs is ~1 μm, and (3) difficulty in the entire end-bonding of the *B*-SWNTs [29] since the *B*-SWNTs are present inhomogeneously in the film.

The present results assure that further optimized *B* doping into CNTs, and forming highly uniform ensemble of the *B*-SWNTs could lead to considerably high T_c (e.g., up to 30 ~ 40 K as in alkali-metal-doped fullerenes and MgB_2). Homogeneously assembled *B*-CNTs, which can provide weakly interacted CNTs (quasi-1D property) so as to maintain both the 1D properties (e.g., contribution of a VHS and strong curvature in one SWNT) and the 3D property (e.g., Meissner shielding-current path across assembled SWNTs), are promising as a novel structure which is expected to open doors to the fields of carbon-based SC.

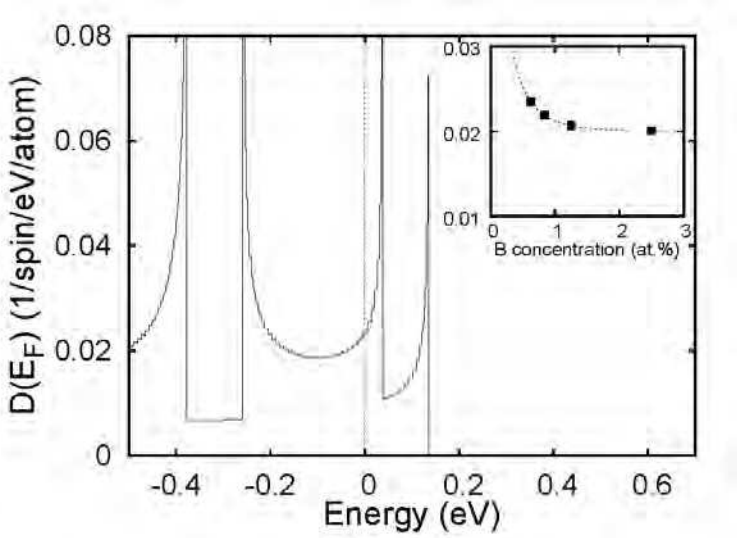

Fig. 12. Electronic density of states of individual *B*-doped semiconducting SWNT, BC_{159} obtained by using the local-density approximation in the framework of the density-functional theory. Plane-wave basis with the cutoff energy of 50 Ry is used. The host CNT is (10, 0) SWNT (i.e., the so-called zigzag nanotube) with the N_B value as low as 0.625 at.%. Energy is measured from the E_F.
Inset: Fermi-level density of states as a function of N_B.

3. Pressure-induced superconductivity at 19 K in boron-doped Buckypapers

As mentioned in section 2, the BCS-type superconductors are expected to exhibit a T_c, because of the high phonon frequency and Debye temperature of carbon atoms with low mass. Recently developed novel carbon-based superconductors (e.g., calcium-intercalated graphite and highly *B*-doped diamond [47–49]) have attracted significant attention from this viewpoint. However, the highest T_c obtained is still now lower than 15 K.
On the other hand, with CNTs, one expects much higher T_c, because (1) the curvature resulting from a small tube diameter (e.g., << 1 nm) can yield a strong coupling between the σ-π electrons and RBM [50, 51] and (2) the alignment of the E_F to a VHS in the electronic DOS (EDOS) can lead to an extremely high electronic density of states [51, 52]. In the sections 1 and 2, I reported SC in the entirely MWNTs [53–55] and in the uniform thin films consisting of *B*--SWNTs [56]. The highest T_c observed in these CNTs, however, is still now 12 K.
In section 2 [56], I showed synthesis of *B*-SWNTs by mixing elemental *B* powder into catalyst in order to intentionally generate charge carriers for SC and assembling them to thin films. We revealed that (1) *B* concentration (N_B) as low as 1.5 atomic % (at.%) and (2) assembling into highly uniform thin films led to Meissner effect with the onset T_c of 12K. I argued that this Meissner effect was realized by (1) the better alignment of E_F to a VHS in the EDOS of the *B*-SWNT [52,56] and (2) providing of a loop current path for Meissner diamagnetism across multiple *B*-SWNTs by the abovementioned two factors, respectively

[54,56]. In these viewpoints, assembling the *B*-SWNTs to film structure is crucial for realizing SC.

Recently, thin films consisting of SWNTs are attracting considerable attention for application to electrically-conductive transparent films and CNT -field effect transistors (FETs) [57]. Thus, thin films of *B*-SWNTs are also highly expected as superconducting transparent films. Here, in study of the above-mentioned previous *B*-SWNT thin films, I had proposed the following measures for increasing T_c: (1) employing lower N_B values (N_B << 1 at.%); (2) using thinner *B*-SWNTs (e.g., diameter << 1 nm); (3) forming a dense assembly of thin films; and (4) applying pressure to the films.

In this section, I show fabrication of paper-like thin films consisting of pseudo two-dimensional network of weakly coupled *B*-SWNTs (the so-called Buckypaper) by sufficiently dissolving as-grown ropes of SWNTs and densely assembling them on silicon substrate. I show T_c of 8K under absent pressure in the Buckypaper and find enhancement of the onset T_c up to 19 K by applying only a small pressure. An increase in the phonon frequency of the radial breathing phonon mode under applied pressure is also found and its correlation with the pressure-induced T_c is discussed.

B-SWNTs were synthesized by the pulsed laser vaporization technique [56], in which N_B was controlled by the amount of elemental *B* mixed with the Co/Ni-catalyst-impregnated targets. Substitutional *B* doping was confirmed by NMR (JNM-ECX400) and Raman spectra measurements. Conventional thin film samples of *B*-SWNTs and the present *B*-Buckypaper were prepared by solubilizing the *B*-SWNTs in dichloroethane solution with densities of 0.5–1 mg/mL and 3–5 mg/mL by centrifugation at 5000 rpm for 1 day and 10000 rpm for 2 days (Tomy; low-speed centrifuge) and ultrasonification (As One, US cleaner) for 2 days and 5 days, respectively. Then, the solutions were spin coated at 500 rpm on a Si substrate.

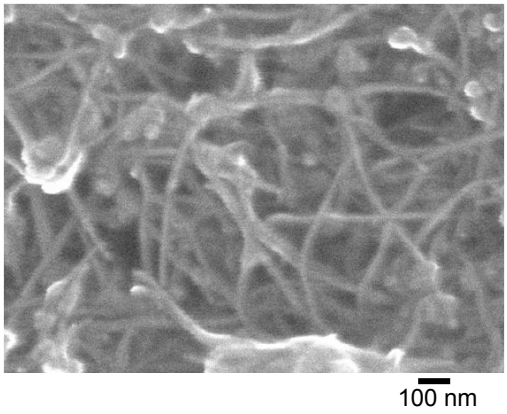

Fig. 13. (a) Top-view FESEM images of the conventional *B*-SWNT thin film fabricated by the conditions following our previous method. It consists of ropes of SWNTs.

Figure 13(a) shows the top-view field-emission scanning electron microscope (FESEM) images of the *B*-SWNTs thin films prepared by a previously reported method [56]. Although we tried to fabricate uniform thin films with dissolving ropes by the previous conditions, Fig. 13(a) reveals that the film still consists of thin ropes of as-grown *B*-SWNTs with ~10 nm diameter.